Research Square

Preprints are preliminary reports that have not undergone peer review.
They should not be considered conclusive, used to inform clinical practice,
or referenced by the media as validated information.

Characterizing Alzheimer's disease with reservoir computing

Jian Gao

gao.jian@bupt.edu.cn

Beijing University of Posts and Telecommunications

Qing Li

Zijian Wang

Yihe Zhang

Zixiang Yan

Xingang Wang

Shaanxi Normal University https://orcid.org/0000-0002-6851-0109

Yong Liu

Beijing University of Posts and Telecommunications https://orcid.org/0000-0002-1862-3121

Jinghua Xiao

Article

Keywords:

Posted Date: July 24th, 2025

DOI: https://doi.org/10.21203/rs.3.rs-7079997/v1

License: This work is licensed under a Creative Commons Attribution 4.0 International License.
Read Full License

Additional Declarations: There is **NO** Competing Interest.

Characterizing Alzheimer's disease with reservoir computing

Qing Li,[1] Zijian Wang,[1] Yihe Zhang,[2] Zixiang Yan,[1] Jian Gao,[1,3] Xingang Wang,[4] Yong Liu,[2] and Jinghua Xiao[1]

[1)] *School of Physical Science and Technology, Beijing University of Posts and Telecommunications, Beijing, China, 100876*

[2)] *School of Artificial Intelligence, Beijing University of Posts and Telecommunications, Beijing, China, 100876*

[3)] *State Key Laboratory of Information Photonics and Optical Communications, Beijing University of Posts and Telecommunications, Beijing, China, 100876*

[4)] *School of Physics and Information Technology, Shaanxi Normal University, Xi'an, China, 710062*

(*Electronic mail: gao.jian@bupt.edu.cn)

(Dated: 9 July 2025)

Alzheimer's disease (AD) is a neurodegenerative disorder characterized by impairments in memory, cognition, and behavior. Resting-state functional magnetic resonance imaging (rs-fMRI) is one of the valuable techniques for studying brain function in AD, providing insights into neural mechanisms and aiding early diagnosis. Traditional rs-fMRI analyses, such as dynamic functional connectivity and time series analysis, aim to explore spatiotemporal relationships between brain regions. However, the short duration of real-world rs-fMRI data often limits their ability to capture nonlinear features that are critical for early-stage AD detection. To overcome these obstacles, this study develops a surrogate model based on the techniques of reservoir computing and compressed sensing (CS-RC), which expands data through time series predictions and extracts nonlinear dynamical characteristics of AD. Two indicators are further proposed based on the developed model, the maximum Lyapunov exponent and the phase locking values, indicating a reduced dynamical complexity in AD and the key AD-affected brain regions in the frontal and parietal lobes, respectively. The classification accuracy based on these two indicators can reach as high as 87% across different datasets, validating the CS-RC analysis approach. Our framework improves the use of rs-fMRI data and may support further theoretical investigations in neurodegenerative disease research.

Introduction

Alzheimer's disease (AD) is a neurodegenerative disorder and the most prevalent form of dementia. Its primary characteristics include memory impairment, cognitive decline, and alterations in behavior, which ultimately result in the inability to carry out daily activities. AD has a devastating impact, adversely affecting patients, their families, and society as a whole. Investigating the underlying mechanisms of AD and improving early detection methods are crucial to timely intervention and treatment. Such advances can improve patients' quality of life, which in turn mitigates social and economic burdens, and ultimately accelerates scientific research and drug development.[1–5]

Recent advances in imaging techniques have provided comprehensive tools for investigating the mechanisms underlying AD.[6] Magnetic resonance imaging (MRI) has unveiled that AD is accompanied with atrophy in various brain regions, including the hippocampus, the entorhinal cortex, and the temporal lobes.[7] The positron emission tomography (PET) imaging technique employs various tracers to identify the atypical aggregation of β-amyloid and tau proteins.[8] These imaging modalities provide significant insight into the pathophysiology of AD from the aspects of structural, metabolic, and molecular changes.

In parallel to other imaging modalities, resting-state functional magnetic resonance imaging (rs-fMRI) characterizes the spatiotemporal properties of spontaneous low-frequency oscillations (0.01-0.1Hz) in brain activity through a moderate temporal resolution (TR=0.5–3s). It captures functional connectivity between different brain regions by measuring blood oxygen level-dependent (BOLD) signals in the absence of specific tasks.[9,10] Existing rs-fMRI studies have provided significant insight into the disrupted connectivity patterns associated with AD.[11–17] Using seed-based analysis, researchers have identified disrupted connectivity in the hippocampus, which is closely related to early memory impairments. Independent component analysis has been used to reveal abnormalities in large-scale networks, particularly the default mode network, a hallmark of AD.[18] Graph-theoretical analyzes further demonstrate that the AD brain exhibits reduced clustering, increased path lengths, and a degradation of the small world topology, indicating a shift toward a more random and inefficient network structure.[19] These findings are strongly correlated with cognitive decline and provide valuable information on the progression of AD.

Dynamic analysis based on rs-fMRI data is another promising approach for AD diagnosis. Compared to static-image-based methods, it better characterizes the brain's temporal dynamics and reveals pathological mechanisms.[20] Current analyses of dynamic information in rs-fMRI predominantly rely on two methodological approaches: dynamic functional connectivity (dFC) and time series analysis[46]. The dFC approach, typically implemented using sliding window correlation techniques, captures time-varying connectivity patterns between brain regions. However, since it relies on linear correlation metrics, dFC may fail to capture nonlinear interactions in neural activity. In contrast, time series analysis methods, such as spectral analysis, Granger causality analysis, and higher-order statistics, offer complementary insights, but they require high-quality, long-duration scans to provide reliable estimates due

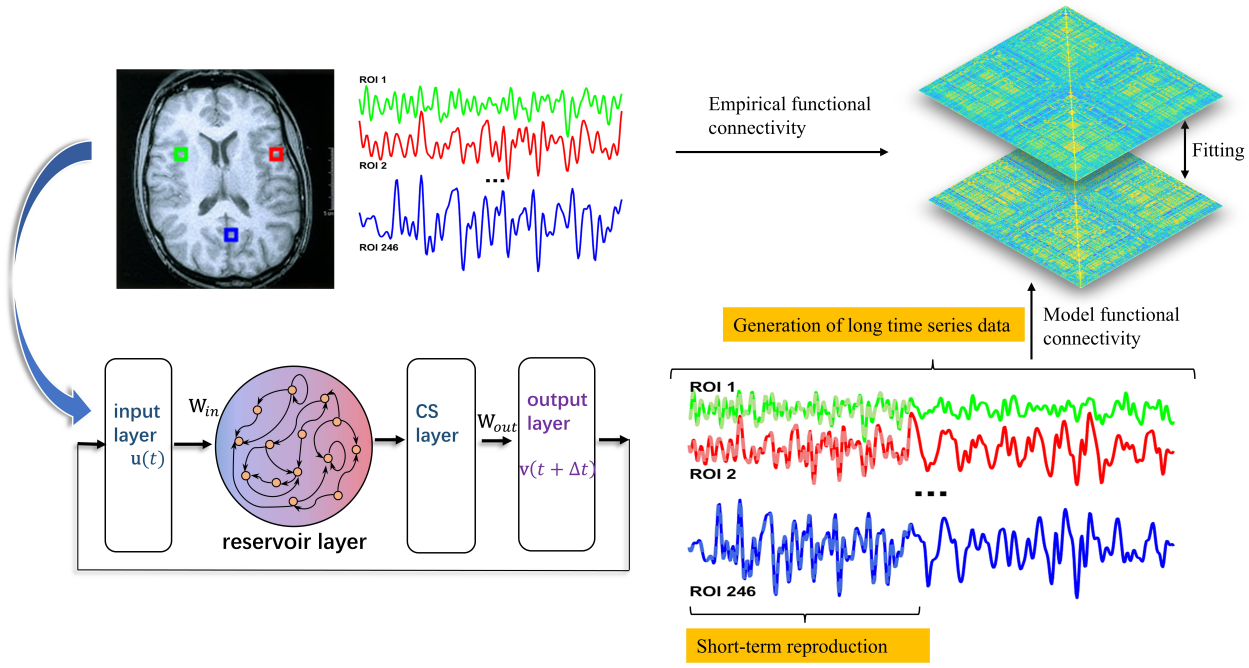


FIG. 1. **The modeling process of CS-RC for rs-fMRI data.** The brain image (upper left) highlights regions of interest (ROIs), with corresponding time series shown above. During the training phase, the time series are mapped through the input layer to the reservoir layer and compression layer. The output matrix is obtained through ridge regression, the model enters a closed-loop evolution, continuously generating new data. The output time series (bottom right) not only reproduce the training data in the short term but also generate long time series data, while preserving the original functional relationships in the data.

to their sensitivity to data characteristics.

In this paper, we propose reservoir computing[23] (RC) as a novel computational framework for characterizing the spatiotemporal complexity of brain functional dynamics, with specific applications to neurodegenerative disorders such as AD. RC is a type of recurrent neural network that can be directly trained on physiological and behavioral data, effectively approximating the dynamics of an underlying system of differential equations.[24,25] In this way, it extracts the underlying dynamical representations from temporal observations and generates realiable following evolutions.[26–29] The high-dimensional state space of RC makes it particularly suitable for modeling complex spatiotemporal data[30]. Furthermore, research indicates that the design of RC inherently possesses the ability to overcome noise interference and data missing problems.[31] After training from temporal observations, the dynamics of the RC serves as a digital twin of the unknown system[32], from which one can calculate various dynamic indicators from RC to characterizing the original unknown system[26].

In this study, we employ Reservoir Computing with Compressed Sensing(CS-RC) for dynamical analysis within the rs-fMRI time series of individuals diagnosed with AD. Upon completion of the CS-RC learning process, the model performs proficiently as an equation-based surrogate for the rs-fMRI data. The surrogate model provides two notable advantages. Firstly, it establishes a well-defined equation that facilitates nonlinear dynamic analysis and the derivation of global dynamical metrics. By calculating the maximum Lyapunov exponent, we find that the overall complexity in individuals with AD is lower than in healthy individuals. Secondly, the CS-RC approach enables long-term autonomous evolution, which allows for the generation of extended data sets, thereby supporting more robust time series analysis. By quantifying inter-regional synchronization using the phase locking value (PLV), we find key AD-affected brain regions. Both our proposed method and the two indicators derived from CS-RC are validated through their performance in an AD classification task.

Results

Reconstructing dynamics from rs-fMRI data. The data used in this study included 489 participants (including 253 AD patients and 236 healthy comparison individuals) from the Multi-Center Alzheimer Disease Imaging Consortium (MCADI) dataset. Detailed information regarding data acquisition and processing protocols can be found in the Methods section. For each subject, the preprocessed rs-fMRI data

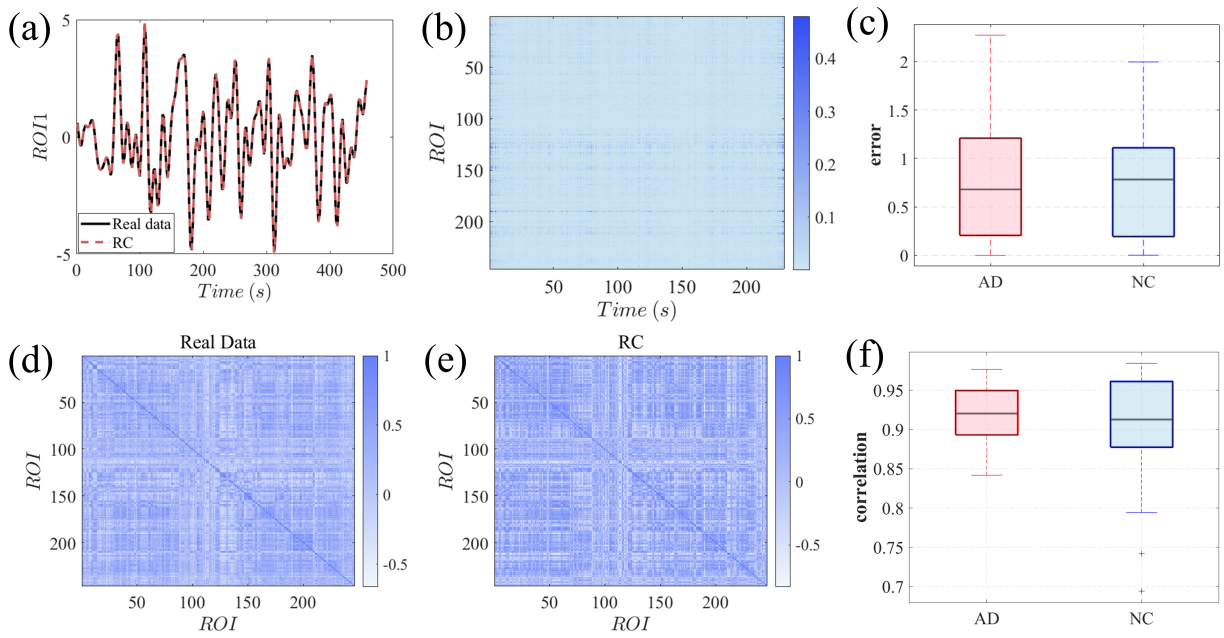


FIG. 2. **The dynamic reconstruction results of CS-RC for rs-fMRI data.** Including the short-term time series reconstruction errors and the maintenance of long-term functional correlations, are obtained from the dataset of Center 1. **a** shows the reconstruction result of one specific time series from the rs-fMRI data of an individual, here, the black solid line represents the real data, and the red dashed line represents the data generated by the model. **b** is a heatmap depicting the reconstruction errors of all time series in the rs-fMRI data of an individual. **c** presents the distribution maps of short-term time series reconstruction errors of NC and AD data. **d** is the functional connectivity matrix obtained by performing Pearson correlation on the real data. **e** is the functional connectivity matrix obtained from the long-term time series generated by CS-RC. **f** shows the distribution maps of the correlation fitting of the functional connectivity matrices between the long-term time series generated by CS-RC and the real time series.

$\boldsymbol{S} \in \mathbb{R}^{N\times L}$ is represented as a matrix in which the k-th column corresponds to the variations in blood oxygenation for the k-th brain region over the scanning period of $L = 230$ time points. Subsequently, the matrix $\boldsymbol{S}$ is input into the reservoir and subsequently processed through the compression layer, as illustrated in Fig. 1. The characteristics of the original reservoir state $\boldsymbol{r}$ are extracted to produce $\boldsymbol{r}_c$, which is utilized to train the output layer as described in Methods. The size of CS-RC is calculated as $cn = 0.1 \times 500 = 50$. All other parameters are optimized during validating stage, with the validation criterion being that the functional connectivity between predicted sequences from CS-RC must closely match that of the ground-truth rs-fMRI data. For each subject, an individualized model was independently trained and evaluated using subject-specific data, with hyperparameters separately optimized for each case.

After training the output weigths $\boldsymbol{W}_{out}$, we substitute the input vector $\mathbf{u}$ with the output vector $\mathbf{v}$ and get the surrogate model for rs-fMRI as

$$\begin{aligned} \boldsymbol{r}(t+\Delta t) &= (1-\alpha)\boldsymbol{r}(t) + \alpha \tanh[\boldsymbol{A}\boldsymbol{r}(t) + \boldsymbol{W}_{in}\boldsymbol{v}(t)] \\ \boldsymbol{v}(t+\Delta t) &= \boldsymbol{W}_{out}\,[\boldsymbol{u}(t); \Phi\Psi \cdot \boldsymbol{r}(t+\Delta t)] \end{aligned}. \quad (1)$$

The initial state of the reservoir is set to zero and is subsequently driven by the actual data for a time step of $\tau = 1$. Then, CS-RC can begin self-evolution with Eq. (1), as shown in Fig. 1, not only reproducing the training data but also generating new data. As illustrated in Fig. 2(a)-(c), these results suggest that CS-RC effectively reconstructs the temporal dynamics of the rs-fMRI data. Furthermore, the reconstruction of the time series demonstrates that CS-RC effectively captures the temporal features present in the training data.

Since the rs-fMRI data reflect functional connectivity between different regions of the brain, we further examine whether CS-RC has captured interactive relationships between these brain regions. CS-RC is capable of performing closed-loop self-evolution to generate data of arbitrary length during the prediction stage. As shown in Fig. 1, after reproducing the first 230 data points, CS-RC can autonomously evolve to generate additional data, extending the time series by 2000 steps, thereby generating a new functional connectivity network. As shown in Fig. 2(e), the functional connectivity network refers to a correlation matrix obtained by computing the Pearson correlation between the newly generated time series. To evaluate how accurately CS-RC reproduces

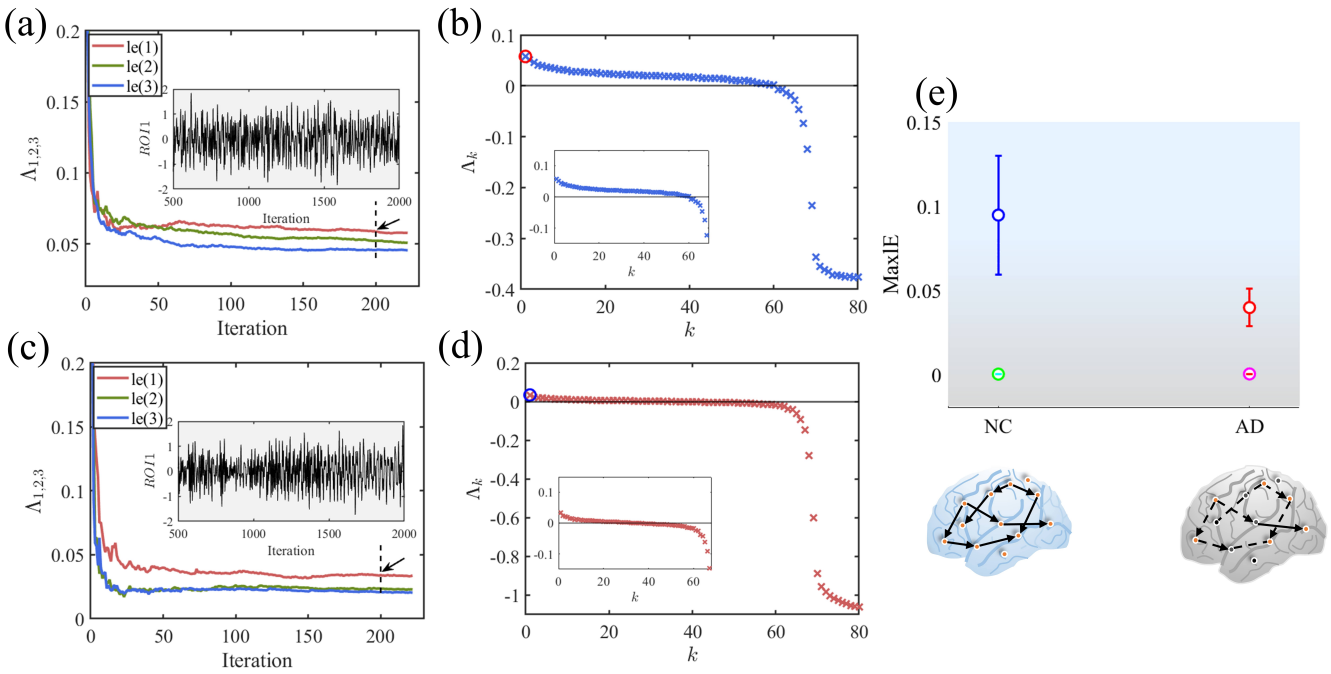


FIG. 3. **Lyapunov exponent analysis of reservoir computing in normal control and Alzheimer's disease groups, are obtained from the dataset of Center 1.** **a** and **c**, evolution of the first three largest Lyapunov exponents across iterations in the NC group **a** and AD group **c**, with corresponding reservoir outputs shown as inset plots. **b** and **d**, the Lyapunov exponent spectra for NC **b** and AD **d** groups, illustrating differences in stability properties. **e** Distribution of the maximum Lyapunov exponents across all datasets. The blue and red colors represent the distribution of the maximum Lyapunov exponents for the AD and NC datasets, respectively, computed using CS-RC. The green and pink colors correspond to the results obtained by estimating the Lyapunov exponents for real rs-fMRI data using Rosenstein's method.

brain functional connectivity, we compute the Pearson correlation between the functional connectivity matrices derived from CS-RC-generated time series and those from the original training data. As shown in Fig. 2(f), for all subjects, the correlation exceeds 0.9, further illustrating that CS-RC captures the temporal characteristics and interaction patterns in the fMRI time series data.

The results demonstrate that the CS-RC characterized the inherent dynamics of the time series, particularly regarding the variation patterns and interactions among different regions of the brain. These results imply that the derived surrogate equation could potentially represent some aspects of the underlying dynamics in the rs-fMRI data. Using the dynamics of CS-RC Eq. (1), we can investigate AD from a dynamic perspective, thereby deepening our understanding of AD.

The dynamic indicators of Alzheimer's disease. We have developed a surrogate model Eq. (1) for rs-fMRI using CS-RC, a dynamical system described by explicit equations, which facilitates the extraction of underlying dynamical characteristics. Most prior studies on AD have employed data-driven approaches. However, these approaches are constrained by the limitations of rs-fMRI data, which mainly supports correlation analyses with statistical significance. In contrast, with the acquisition of a surrogate equation, various dynamic analyses become feasible.

For complicated non-linear dynamical systems, the Lyapunov exponents is a quantitative measure of chaotic behavior, system complexity, and dynamic stability.[40,41] In the context of AD, calculating Lyapunov exponents from a surrogate model enables the detection of subtle yet informative changes in brain dynamics, reflecting alterations in both stability and complexity associated with disease progression. These changes reflect impaired brain information processing and loss of dynamical complexity, which are hallmark features of AD pathophysiology. Moreover, the dynamic analysis of Lyapunov exponents provides insight into the pathological progression of AD, offering a more nuanced perspective on the disease's underlying mechanisms compared to traditional correlation-based analyses.

From the surrogate model Eq. (1), the reservoir represents a discrete-time dynamical system of dimension $\boldsymbol{D}_r$. To compute the Lyapunov exponents, we first derive the evolution equations for the corresponding tangent map, as described in Eq. 2

$$\boldsymbol{\delta r}(t+\Delta t) = \boldsymbol{J}\cdot\boldsymbol{\delta r}(t). \tag{2}$$

Here, $\boldsymbol{J}$ represents the Jacobian matrix of the system evolution equation (see Methods for details). A set of m

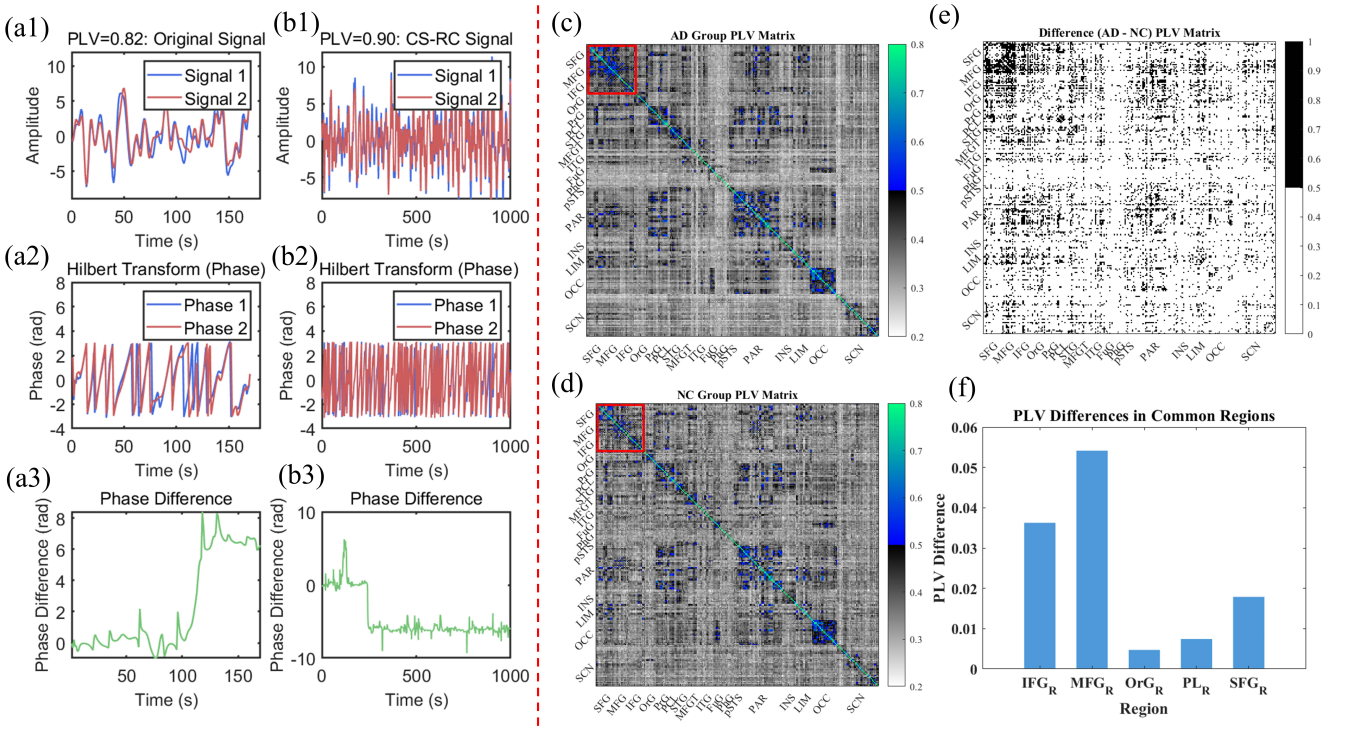


FIG. 4. **Phase-Locking Value (PLV) Analysis Between AD and NC Groups (Center 1 Dataset). (a1-b1)** Original BOLD signals from two brain regions (PLV = 0.82) and corresponding CS-RC signals (PLV = 0.90), showing enhanced synchronization. **(a2-b2)** Phase comparison using Hilbert transform for original and CS-RC signals. **(a3-b3)** Phase difference over time for original vs. CS-RC signals, with CS-RC showing more stable phase synchronization. **c** PLV matrix for the AD group, where blue indicates stronger synchronization and green weaker; red box highlights high-synchronization regions. **d** PLV matrix for the NC group using the same color scale. **e** PLV difference matrix (AD-NC), with black and white indicating the magnitude of differences in synchronization. **f** Bar plot of PLV differences between AD and NC groups across several brain regions: Inferior Frontal Gyrus, Middle Frontal Gyrus, Orbital Gyrus, Parietal Lobe, and Superior Frontal Gyrus.

mutually orthogonal tangent vectors is denoted by $\boldsymbol{R}(t) = [\boldsymbol{\delta r}_1(t), \boldsymbol{\delta r}_2(t), \ldots, \boldsymbol{\delta r}_m(t)]$, where each $\boldsymbol{\delta r}_j(t)$ represents a tangent vector at time t. The largest m Lyapunov exponents of the reservoir dynamical system are computed by analyzing the time evolution of the matrix $\boldsymbol{R}(t)$ using a standard $\boldsymbol{QR}$ decomposition algorithm[42]. Specifically, at each time step, the matrix $\boldsymbol{R}(t)$ is decomposed into an orthogonal matrix $\boldsymbol{Q}(t)$ and an upper triangular matrix $\boldsymbol{U}(t)$. The Lyapunov exponents are extracted by examining the diagonal elements of the matrix $\boldsymbol{U}(t)$, with the largest exponents corresponding to the divergence rates of the tangent vectors. These exponents provide information about the stability and chaotic behavior of the system.

The analysis of Lyapunov exponents derived from CS-RC highlights significant reductions in brain dynamic complexity among Alzheimer's disease patients compared to normal controls. The convergence of the three largest Lyapunov exponents indicates that both the NC and AD groups reach stable dynamic states after sufficient iterations (Fig. 3a, c). However, the stable Lyapunov exponent values differ significantly, with the AD group exhibiting systematically lower values. Quantitative comparisons of the maximum Lyapunov exponents (MaxLE) clearly illustrate that AD patients possess significantly lower dynamic complexity compared to NC (Fig. 3e). These dynamical characteristics are aligned with the pathological progression of AD, reflecting reduced network complexity.[43] The MaxLE serves as a sensitive dynamical marker to capture neural alterations related to AD.

In addition to dynamic indicators, the surrogate model could be used to generate more data to analyze. The original rs-fMRI time series typically have around $100-200$ time steps, and such short time series are susceptible to random noise or individual variability, resulting in instability and reduced reliability in statistical analyzes. Many of the synchronization metrics traditionally used in functional connectivity analyzes are also limited by these short time series, which often lack sufficient data to yield reliable results. However, by using CS-RC, we can generate new data that extend the length of the original time series by at least tenfold, making the computed synchronization metrics more reliable.

In this paper, we take the Phase Locking Value (PLV) as an example, which is the key synchronization metrics that quantifies the degree of phase synchronization between different regions of the brain[44]. PLV is particularly valuable because it provides a direct, robust measure of temporal coherence in brain activity, helping to identify regions with abnormal

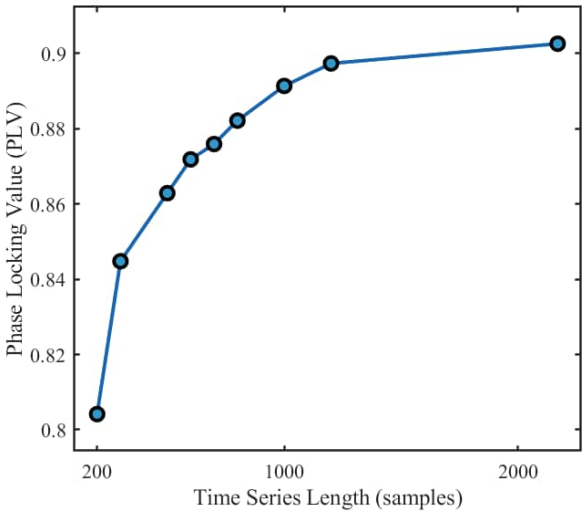


FIG. 5. **Influence of Time Series Length on Phase Locking Value.** The PLV stabilizes with increasing sequence length, demonstrating that longer time series provide more reliable phase synchronization measurements.

synchronization patterns. These regions may exhibit reduced complexity, which can be indicative of dysfunction or pathological changes. As a synchronization metric, PLV serves as a reliable tool for pinpointing abnormal areas with reduced complexity, offering deeper insights into the dynamics of the brain network.

PLV is calculated by first extracting the instantaneous phase of each signal using the Hilbert transform, as illustrated in panels Fig. 4(a2) and (b2). After obtaining the instantaneous phases, the phase difference between the two signals is computed at each discrete time point. As illustrated in Fig. 4(a3) and (b3), the use of CS-RC allows extension of the data. Longer time series provide more signal features, allowing the PLV to more accurately reflect synchronization, as shown in Fig. 5. Consequently, the calculated phase difference is more stable compared to that derived from shorter data sets. These phase differences are then represented as complex exponentials $e^{i\Delta\phi(t)}$, where $\Delta\phi(t)$ denotes the phase difference between signals at time t. The PLV is subsequently computed as

$$PLV = \left| \frac{1}{N} \sum_{t=1}^{N} e^{i\Delta\phi(t)} \right|, \tag{3}$$

with a range spanning from 0 to 1, reflecting the incoherence to synchrony. N-dimensional channels can be divided into M brain regions, as shown in Fig. 4(c-d). The PLV matrix is obtained by calculating the average of the PLV among all subject signals. As shown in Fig. 4(e-f), the PLV values of AD in the frontal and parietal lobes are significantly higher than those of NC, reflecting the decrease in complexity of these regions. The reduction in joint complexity may indicate functional changes in the multiregional networks of the brains of AD patients. This decline in complexity is likely closely associated with a deterioration in cognitive functions, particularly in terms of memory, spatial navigation, and executive functions.

Based on the surrogate model for rs-fMRI data through CS-RC, we obtain the dynamical indicator MaxLE for the global measure of complexity and the statistic indicator PLV for phase synchronization at a local scale. The CS-RC offers a versatile framework for studying complex brain dynamics of rs-fMRI data.

Classification of Alzheimer's disease. The validation of the CS-RC-based indicators could be checked through the AD classification task. Recently developed methods for AD classification using rs-fMRI data have shown varying degrees of success with various methods. Focusing on rs-fMRI data, permutation entropy (PE) as a computationally efficient measure to detect changes in brain dynamics has been used in previous studies[45]. Due to the limitation of rs-fMRI data, although PE has demonstrated potential for AD detection, its performance in classification tasks remains limited, as shown in our experiments, where PE achieved a classification accuracy of only 51.7% (Fig.6 a). In addition, deep learning models[46], such as C3D-LSTM[47], which process 4D spatio-temporal data using 3D CNNs for spatial feature extraction and LSTMs for temporal modeling, offer higher accuracy (97.4%). However, these models are computationally intensive and lack interpretability, which presents challenges for their clinical adoption, where transparency is vital for decision-making. Moreover, unsupervised models like DMACN[48] analyze static functional connectivity using multi-kernel autoencoders and achieve moderate accuracy (71.9%), but suffer from limited clustering accuracy due to the lack of label guidance.

In this paper, we extend PE by incorporating the MaxLE and PLV extracted from prefrontal regions (Superior Frontal Gyrus, SFG) as additional classification features. These indicators effectively capture the dynamic temporal patterns of brain activity, providing an efficient and interpretable approach for AD classification. The classification procedure involves three steps:(1) feature normalization to standardize input features; (2) model training using a support vector machine with a radial basis function kernel, where hyperparameters are automatically tuned via Bayesian optimization; and (3) performance evaluation was conducted using leave-one-out cross-validation.

The classification results, shown in Fig.6(b), demonstrate that the proposed CS-RC-based indicators achieve classification accuracies ranging from 60.0% to 87.5% across datasets from six centers. Although the accuracy is lower than that of more complex models such as C3D-LSTM (which achieved 97.4%), our method offers competitive performance while maintaining lower computational cost and greater interpretability. Notably, our results are obtained from data collected across six centers, involving a total of 489 subjects, which is substantially larger than most existing studies that typically include only 100 to 200 participants. This broader dataset enhances the robustness and generalizability of our findings, suggesting its potential as an auxiliary diagnostic tool for AD.

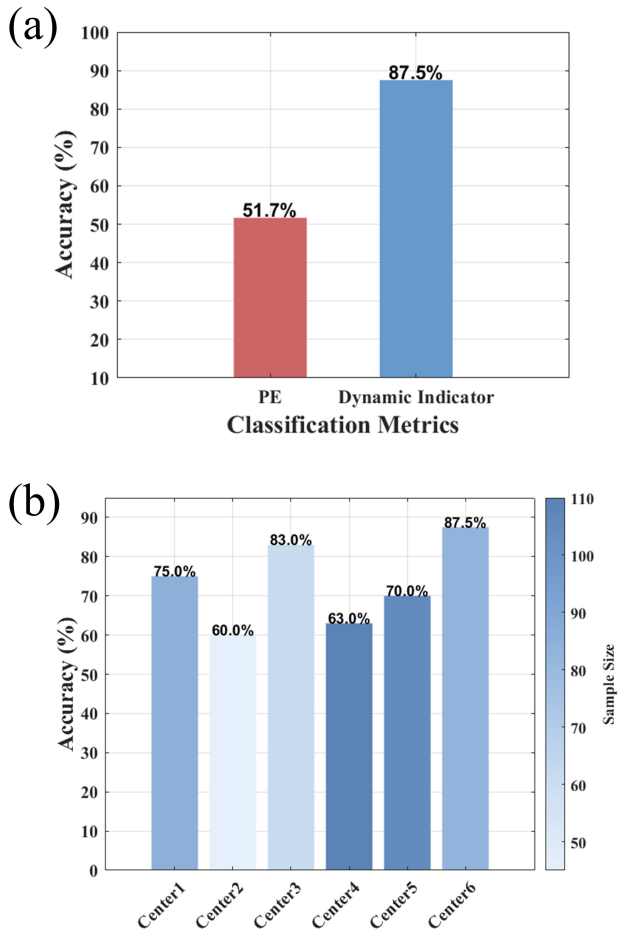


FIG. 6. **Evaluation of the Classification Performance of the Dynamic Indicator.** **a** The bar plot shows the classification accuracy of the two indicators on the dataset from Center 1. The accuracy based on PE reaches 51.7%, whereas the proposed dynamic indicator achieves a significantly higher accuracy of 87.5%. **b** The bar plot shows the classification accuracy of the proposed dynamic indicator for AD vs. CN across datasets from six centers. Each bar represents one center, and the height corresponds to the achieved accuracy, while the color indicates the sample size used for classification.

Discussions

In this study, we introduced a surrogate modeling approach based on the CS-RC framework to analyze resting-state functional MRI data in patients with Alzheimer's Disease and normal controls. The CS-RC model demonstrates significant potential as a diagnostic tool by offering both interpretability through explicit dynamical equations and robust data extension capabilities, which collectively enhance the reliability of downstream statistical inference.

Two key dynamical features were extracted using the CS-RC model: MaxLE and PLV. MaxLE serves as an index of global dynamical complexity, while PLV quantifies local phase synchronization. We observed a significant reduction in MaxLE in the AD group, indicating a lower degree of complexity in their neural dynamics. This aligns with previous findings suggesting that AD is associated with the degradation of large-scale integrative dynamics and a shift toward more rigid or hypo-complex brain states. Such reduced complexity reflects a loss of adaptability and functional variability, hallmarks of neurodegeneration.

In parallel, PLV analysis revealed abnormally elevated phase synchronization in specific cortical regions within the AD group, notably in the Inferior Frontal Gyrus, Middle Frontal Gyrus, Orbital Gyrus, Parietal Lobe, and Superior Frontal Gyrus. These regions are critically involved in executive control, working memory, emotional regulation, spatial cognition, and self-referential processing, respectively. The observed increases in local synchrony may reflect maladaptive hyper-synchronization resulting from neuronal loss, disrupted inhibitory-excitatory balance, or impaired long-range connectivity, which in turn leads to reduced network flexibility and functional segregation.

These regional abnormalities occur alongside the observed reduction in MaxLE, which reflects a global decline in the brain's dynamical complexity and integrative capacity. This dual pattern suggests that Alzheimer's disease involves not only widespread disruption of global neural dynamics but also focal reorganization of cortical synchrony, particularly in regions subserving key cognitive and affective functions. Taken together, the complementary roles of MaxLE and PLV offer a more nuanced and comprehensive account of AD-related neurophysiological dysfunction, spanning from macroscale network desynchronization to regional hyper-coupling.

Compared to traditional and deep learning methods, the CS-RC model demonstrates two key advantages. Theoretical Interpretability: Unlike deep neural networks, which often operate as black-box models, the CS-RC framework provides explicit equations that can be analyzed for stability, nonlinearity, and bifurcation behavior. This makes the model particularly valuable for hypothesis generation and clinical explanation. Computational Efficiency: The model offers substantially lower computational cost, allowing fast inference and easier deployment in real-time or near real-time settings, which is especially important in clinical applications where computational resources and latency are constrained.

Despite these advantages, the CS-RC-based indicators (87.5% accuracy) are not as high-performing as deep learning models like C3D-LSTM (97.4%). However, the trade-off is favorable when clinical feasibility, interpretability, and model simplicity are considered. Compared to traditional complexity measures like permutation entropy (PE, 51.7%) or unsupervised architectures like DMACN (71.9%), CS-RC clearly outperforms in both discriminative power and generalizability.

The considerable variation in classification accuracy across centers (ranging from 60.0% to 87.5%) highlights critical limitations in the model's cross-site generalizability. These discrepancies may arise from differences in data acquisition protocols, sample sizes, and population characteristics, underscoring the need for robust domain adaptation strategies and multi-center harmonization techniques. Future work should

explore advanced techniques such as cross-site validation, domain-invariant representation learning, and center-specific normalization to mitigate site-related biases. Furthermore, incorporating uncertainty quantification and interpretability analysis will enhance model reliability and foster clinical trust across diverse deployment environments.

Conclusion

This study used the CS-RC-based surrogate model to analyze rs-fMRI data from AD and NC. The model exhibits two major advantages, as the explicit dynamical equations that enable theoretical analysis, and the data extension capability substantially improving the reliability of statistical indicators. Using this model, we computed the MaxLE index reflecting global complexity and PLV values that characterize local phase synchronization. The significantly lower MaxLE is found in AD patients compared to NC, indicating reduced dynamical complexity of the brain. Furthermore, PLV analysis reveals abnormal patterns of synchronization in specific brain regions in the AD group. While the proposed indicators (87.5%) are less accurate than C3D-LSTM (97.4%), their computational efficiency and interpretability make them more suitable for clinical deployment. In contrast, traditional methods such as PE achieve only 51.7% accuracy, and unsupervised models (e.g., DMACN) perform moderately (71.9%). The CS-RC-based method presents a new approach to AD auxiliary diagnosis, balancing dynamic feature analysis, computational efficiency, and clinical interpretability.

Methods

Participants, data and measurement. This section provides an overview of rs-fMRI acquisition, preprocessing, and quality control. The detailed description of the rs-fMRI data used in this study can be found elsewhere as part of a study investigating altered spontaneous activity in AD.[33,34] The data used in this study included 489 participants (including 253 AD patients and 236 healthy comparison individuals) from the Multi-Center Alzheimer Disease Imaging Consortium (MCADI) dataset. The rs-fMRI were reprocessed using the Brainnetome Toolkit (http://brant.brainnetome.org)[35], which included the following steps: (1) slice timing correction; (2) realignment to the first volume; (3) spatial normalization to the Montreal Neurological Institute (MNI) space at 2mm × 2mm × 2 mm, (4) regression of nuisance signals, including linear trends, six motion parameters and their first-order differences, and signals representing white matter and cerebrospinal fluid; (5) temporal bandpass filtering (0.01-0.08 Hz) to reduce high-frequency noise. Detailed data preprocessing can be found in our previous work[36,37].

The cortex and subcortex were parcellated based on the Brainnetome Atlas. The above preprocessing steps resulted in a set of 246 regional areas of the Brainnetome Atlas, which were used in all further analyses. We derived a regional rs-fMRI signal for each region by averaging the rs-fMRI signal across all voxels included in the region. This process was repeated for all individuals and regions.

Reservoir Computing with Compressed Sensing. CS-RC, proposed by Zhang[38] et al. in 2021, combines compressed sensing and reservoir computing. It can be applied to fields such as time series prediction, and stock data prediction[39]. The CS-RC consists of four modules: input layer, reservoir, compression layer, and output layer. The input layer is characterized by the matrix $\boldsymbol{W}_{in} \in \mathbb{R}^{n\times d}$, whose function is coupling the input vector $\boldsymbol{u}(t) \in \mathbb{R}^d$ to the reservoir. The elements of $\boldsymbol{W}_{in}$ are randomly drawn from a uniform distribution within the range $[-\sigma,\sigma]$. The reservoir is represented by a complex network of n dynamical nodes, with the initial states of the nodes randomly chosen from the interval $[-1,1]$. The state of the reservoir network, $\boldsymbol{r}(t) \in \mathbb{R}^n$, is updated as

$$\boldsymbol{r}(t+\Delta t) = (1-\alpha)\boldsymbol{r}(t) + \alpha \tanh[\boldsymbol{A}\boldsymbol{r}(t) + \boldsymbol{W}_{in}\boldsymbol{u}(t)]. \quad (4)$$

Here, Δt is the time step for updating the reservoir, α is the leaking coefficient, and $\boldsymbol{A} \in \mathbb{R}^{n\times n}$ is a weighted adjacency matrix characterizing the coupling relationship between the nodes in the reservoir. The adjacency matrix $\boldsymbol{A}$ is constructed as a sparse random Erdös-Rényi network: with the probability p, each element of the matrix is arranged with a nonzero value randomly drawn from the interval $[-1,1]$. The matrix $\boldsymbol{A}$ is rescaled to make its spectral radius equal to λ.

An additional compression layer is added in the RC. The compressed layer can facilitate the ability of the RC to capture these sparse features by concentrating on the most significant time intervals and brain regions, thereby uncovering shared characteristics among diverse samples. In addition, it also reduces the dimensionality of the reservoir network, thus enhancing the stability and speed of the model predictions. We assume that the dimension of the original reservoir network is n, and the reduced dimension of CS-RC is cn, where c is the compression ratio. The state of the reservoir network of CS-RC, $\boldsymbol{r}_c(t) \in \mathbb{R}^{cn}$ is obtained by

$$\boldsymbol{r}_c(t+\Delta t) = \Phi\Psi \cdot \boldsymbol{r}(t+\Delta t), \quad (5)$$

where Φ is the measurement marix and Ψ is the sparse matrix. The measurement matrix Φ is constructed by selecting specific rows and columns from the Hadamard matrix to meet the sparse measurement requirements of compressed sensing. The sparse transform matrix Ψ is generated using the discrete wavelet transform, utilizing its multiscale analysis to highlight the sparsity characteristics of the signal, thus optimizing the performance of reconstruction. After the compression layer, r_c is used to train the output layer. The output layer is characterized by the matrix $\boldsymbol{W}_{out} \in \mathbb{R}^{d\times cn}$, which generates the output vector, $\boldsymbol{v}(t) \in \mathbb{R}^d$, according to the equation

$$\boldsymbol{v}(t+\Delta t) = \boldsymbol{W}_{out}\left[\boldsymbol{u}(t); \boldsymbol{r}_c(t+\Delta t)\right]. \quad (6)$$

Unlike $\boldsymbol{A}$ and $\boldsymbol{W}_{in}$, the elements of $\boldsymbol{W}_{out}$ are not given in the construction, but to be "learned" from the input signals through the training process. The purpose of training is to find the proper elements for $\boldsymbol{W}_{out}$ such that the output vector $\boldsymbol{v}(t+\Delta t)$ is as close as possible to $\boldsymbol{u}(t+\Delta t)$ for t $=(\tau+1)\Delta t, \cdots, (\tau+T)\Delta t$,with $T_0 = \tau\Delta t$ the transient period

TABLE I. Hyperparameters of reservoir computing

Parameter	Description	Range
n	the size of the reservoir network	[100, 1000]
p	the connectivity of the reservoir network	[0, 1]
λ	the spectral radius of the reservoir network	[0, 3]
σ	the range defining the input matrix	[0, 3]
α	the leaking coefficient	[0, 1]
η	the ridge regression coefficient	$[10^{-8}, 10^{-3}]$

to avoid the impact of the initial states of the reservoir and T the length of training time series.

We employ the mean squared error as the evaluation metric whose optimal value can be obtained by ridge regression. The output weights $\boldsymbol{W}_{out}$ can be analytically given by

$$\boldsymbol{W}_{out} = \boldsymbol{U}\boldsymbol{V}^T(\boldsymbol{V}\boldsymbol{V}^T + \eta\mathbb{I})^{-1}. \tag{7}$$

Here, $\boldsymbol{V} \in \mathbb{R}^{(d+cn)\times T}$ is the state matrix whose kth column is $[\boldsymbol{u}(\tau+k-1)\Delta t; \boldsymbol{r}_c(\tau+k)\Delta t]$, $\boldsymbol{U} \in \mathbb{R}^{d\times T}$ is a matrix whose kth column is $\boldsymbol{u}[(\tau+k)\Delta t]$, $\mathbb{I}$ is the identity matrix, η is the ridge regression coefficient for overfitting prevention. All hyperparameters (as shown in Table 1) are fixed in the algorithm construction, and each set of hyperparameters generates a unique output matrix. Once the output matrix is obtained, the training phase is completed. The set of hyperparameters and the output matrix together define a specific CS-RC, which will be used later for validation and prediction purposes.

After model training is completed, we optimize the hyperparameters through the following validation process: the similarity between the predicted and true FC matrices is used as the optimization objective. Specifically, the negative correlation coefficient is employed as the validation loss function:

$$\mathscr{L}_{\text{val}}(\boldsymbol{\theta}) = -\rho\left(\mathbf{C}_{\text{pred}}(\boldsymbol{\theta}), \mathbf{C}_{\text{true}}\right) \tag{8}$$

Here, $\boldsymbol{\theta}$ denotes the set of hyperparameters to be optimized. $\mathbf{C}_{\text{pred}}(\boldsymbol{\theta})$ represents the predicted FC matrix generated with the current hyperparameters $\boldsymbol{\theta}$, and $\mathbf{C}_{\text{true}}$ is the ground-truth FC matrix derived from real rs-fMRI data. The function $\rho(\cdot,\cdot)$ computes the Pearson correlation coefficient between two matrices. The optimization criterion is to minimize the negative correlation (i.e., maximize the consistency between predicted and true FC), guiding the hyperparameter search.

Jacobian Matrix in CS-RC. The dynamical equations of the reservoir computing with compressed sensing in the self-feedback evolution stage are:

$$\begin{cases} \boldsymbol{r}(t+\Delta t) = (1-\alpha)\boldsymbol{r}(t) + \alpha\tanh\left[\boldsymbol{A}\boldsymbol{r}(t) + \boldsymbol{W}_{in}\boldsymbol{v}(t)\right] \\ \boldsymbol{v}(t+\Delta t) = \boldsymbol{W}_{out}\left[\boldsymbol{v}(t); \Phi\Psi\cdot\boldsymbol{r}(t+\Delta t)\right] \end{cases}. \tag{9}$$

Based on the above dynamical equations, we obtain the Jacobian matrix as follows:

$$J = \begin{pmatrix} \frac{\partial \boldsymbol{r}(t+\Delta t)}{\partial \boldsymbol{r}(t)} & \frac{\partial \boldsymbol{r}(t+\Delta t)}{\partial \boldsymbol{v}(t)} \\ \frac{\partial \boldsymbol{v}(t+\Delta t)}{\partial \boldsymbol{r}(t)} & \frac{\partial \boldsymbol{v}(t+\Delta t)}{\partial \boldsymbol{v}(t)} \end{pmatrix}$$

$$= \begin{pmatrix} (1-\alpha)+\alpha\cdot df\cdot\boldsymbol{A} & \alpha\cdot df\cdot\boldsymbol{W}_{in} \\ \boldsymbol{W}_{out,2}\cdot\Phi\Psi\left[(1-\alpha)+\alpha\cdot df\cdot\boldsymbol{A}\right] & \boldsymbol{W}_{out,1}+\boldsymbol{W}_{out,2}\cdot\Phi\Psi\alpha\cdot df\cdot\boldsymbol{W}_{in} \end{pmatrix}. \tag{10}$$

Here, $df = 1-\tanh^2[\boldsymbol{A}\boldsymbol{r}(t) + \boldsymbol{W}_{in}\boldsymbol{v}(t)]$.

Acknowledgments

This work was supported by the National Natural Science Foundation of China (NNSFC) under Grant No. 62333002 and Opening Project of State Key Lab of Information Photonics and Optical Communications under Grant No. IPOC2023ZJ02, and the Fundamental Research Funds for the Central Universities under Grant No. 2024RC11.

References

[1] B. N. Dugger and D. W. Dickson, Pathology of Neurodegenerative Diseases, Cold Spring Harbor Perspect. Biol **9** , a028035(2017).

[2] H. M. Snyder, R. A. Corriveau, S. Craft, J. E. Faber, S. M. Greenberg, D. Knopman, B. T. Lamb, T. J. Montine, M. Nedergaard *et al.*, Vascular contributions to cognitive impairment and dementia including Alzheimer's disease, Alzheimers Dement. **10**, 1 (2014).

[3] C. A. Lane, J. Hardy and J. M. Schott, Alzheimer's disease, Eur. J. Neurol. **25**, 59 (2018).

[4] A. P. Porsteinsson, R. S. Isaacson, S. Knox, M. N. Sabbagh, and I. Rubino, Diagnosis of Early Alzheimer's Disease: Clinical Practice in 2021, J Prev Alzheimers Dis **8**, 371 (2021).

[5] X.-X. Zhang, Y. Tian, Z.-T. Wang, Y.-H. Ma, L. Tan, and J.-T. Yu, The Epidemiology of Alzheimer's Disease Modifiable Risk Factors and Prevention, J Prev Alzheimers Dis **8**, 313 (2021).

[6] A. Chandra, G. Devenoulas, M. Politis, Magnetic resonance imaging in Alzheimer's disease and mild cognitive impairment, J. Neurol. **269**, 1293 (2019).

[7] L. Pini, M. Pievani, M. Bocchetta, D. Altomare, P. Bosco, E. Cavedo, S. Galluzzi, M. Marizzoni, G. B. Frisoni, Brain atrophy in Alzheimer's Disease and aging, Ageing Res. Rev. **30**, 25 (2016).

[8] J. Ye, H. Wan, S. Chen, G.-P. Liu, Targeting tau in Alzheimer's disease: from mechanisms to clinical therapy, Neural Regen Res **19**, 1489 (2024).

[9] B. Ibrahim, S. Suppiah, N. Ibrahim, M. Mohamad, H. Abu Hassan, N. S. Nasser, M. I. Saripan, Diagnostic power of resting-state fMRI for detection of network connectivity in Alzheimer's disease and mild cognitive impairment: A systematic review, Hum. Brain Mapp. **42**, 2941 (2021).

[10] T. O. Laumann, A. Z. Snyder, A. Mitra, E. M. Gordon, C. Gratton, B. Adeyemo, A. W. Gilmore, S. M. Nelson, J. J. Berg *et al.*, On the Stability of BOLD fMRI Correlations, Cereb. Cortex **27**, 4719 (2017).

[11] Y. Liu, K. Wang, C. Yu, Y. He, Y. Zhou, M. Liang, L. Wang, T. Jiang, Regional homogeneity, functional connectivity and imaging markers of Alzheimer's disease: A review of resting-state fMRI studies, Neuropsychologia **46**, 1648 (2008).

[12] R. Jing, P. Chen, Y. Wei, J. Si, Y. Zhou, D. Wang, C. Song, H. Yang, Z. Zhang *et al.*, Altered large-scale dynamic connectivity patterns in Alzheimer's disease and mild cognitive impairment patients: A machine learning study, Hum. Brain Mapp. **44**, 1 (2023).

[13] P. Chen, H. Yao, B. M. Tijms, P. Wang, D. Wang, C. Song, H. Yang, Z. Zhang *et al.*, Four distinct subtypes of Alzheimer's disease based on resting-state connectivity biomarkers, Biol. Psychiatry **93**, 759 (2023).

[14] D. Jin, P. Wang, A. Zalesky, B. Liu, C. Song, D. Wang, K. Xu, H. Yang, Z. Zhang, H. Yao, B. Zhou *et al.*, Grab-AD: Generalizability and reproducibility of altered brain activity and diagnostic classification in Alzheimer's disease, Hum. Brain Mapp. **41**, 3379 (2020).

[15] D. Wang, Z. Li, K. Zhao, P. Chen, F. Yang, H. Yao, B. Zhou, Y. Wei, J. Lu, Y. Chen, X. Zhang, Y. Han, P. Wang, Y. Liu, Macroscale gradient dysfunction in Alzheimer's disease: Patterns with cognition terms and gene expression profiles, Hum. Brain Mapp. **45**, e70046 (2024).

[16] D. Jin, B. Zhou, Y. Han, J. Ren, T. Han, B. Liu, J. Lu, C. Song, P. Wang, D. Wang, J. Xu, Z. Yang *et al.*, Generalizable, reproducible, and neuroscientifically interpretable imaging biomarkers for Alzheimer's disease, Adv. Sci. **7**, 2000675 (2020).

[17] K. Zhao, D. Wang, D. Wang, P. Chen, Y. Wei, L. Tu, Y. Chen, Y. Tang, H. Yao, B. Zhou, J. Lu, P. Wang, Z. Liao, Y. Chen, Y. Han, X. Zhang, Y. Liu,

Macroscale connectome topographical structure reveals the biomechanisms of brain dysfunction in Alzheimer's disease, Sci. Adv. **10**, eado8837 (2024).
[18]M. J. Jafri, G. D. Pearlson, M. Stevens, V. D. Calhoun, A method for functional network connectivity among spatially independent resting-state components in schizophrenia, NeuroImage **39**, 1666 (2008).
[19]V. M. Eguíluz, D. R. Chialvo, G. A. Cecchi, M. Baliki, A. V. Apkarian, Scale-Free Brain Functional Networks, Phys. Rev. Lett. **94**, 018102 (2005).
[20]L. Yang, J. Lu, D. Li, J. Xiang, T. Yan, J. Sun, B. Wang, Alzheimer's Disease: Insights from Large-Scale Brain Dynamics Models, Brain Sci **13**, 1133 (2023).
[21]E. L. Dennis and P. M. Thompson, Functional Brain Connectivity Using fMRI in Aging and Alzheimer's Disease, Neuropsychol. Rev. **24**, 49 (2014).
[22]S. L. Warren and A. A. Moustafa, Functional magnetic resonance imaging, deep learning, and Alzheimer's disease: A systematic review, J. Neuroimaging **33**, 5 (2023).
[23]H. Jaeger and H. Haas, Harnessing nonlinearity: Predicting chaotic systems and saving energy in wireless communication, Science **304**, 78 (2004).
[24]Z. Lu, J. Pathak, B. Hunt, M. Girvan, R. Brockett, and E. Ott, Reservoir observers: Model-free inference of unmeasured variables in chaotic systems, Chaos **27**, 041102 (2017).
[25]H. Zhang, H. Fan, L. Wang, and X. G. Wang, Learning Hamiltonian dynamics with reservoir computing, Phys. Rev. E **104**, 024205 (2021).
[26]J. Pathak, Z. Lu, B. Hunt, M. Girvan, and E. Ott, Using machine learning to replicate chaotic attractors and calculate Lyapunov exponents from data, Chaos **27**, 121102 (2017).
[27]Y. Du, Q. Li, H. Fan, M. Zhan, J. Xiao, and X. Wang, Inferring attracting basins of power systems with machine learning, Phys. Rev. Res. **6**, 013181 (2024).
[28]H. Luo, Y. Du, H. Fan, X. Wang, J. Guo, and X. Wang, Reconstructing bifurcation diagrams of chaotic circuits with reservoir computing, Phys. Rev. E **109**, 024210 (2024).
[29]L. Wang, H. Fan, Y. Wang, J. Gao, Y. Lan, J. Xiao, and X. Wang, Inferring synchronizability of networked heterogeneous oscillators with machine learning, Phys. Rev. E **107**, 024314 (2023).
[30]J. Pathak, B. Hunt, M. Girvan, Z. Lu, and E. Ott, Model-free prediction of large spatiotemporally chaotic systems from data: A reservoir computing approach, Phys. Rev. Lett. **120**, 024102 (2018).
[31]Z.-M. Zhai, L.-W. Kong, and Y.-C. Lai, Emergence of a resonance in machine learning, Phys. Rev. Res. **5**, 033127 (2023).
[32]L.-W. Kong, Y. Weng, B. Glaz, M. Haile, Y.-C. Lai, Reservoir computing as digital twins for nonlinear dynamical systems, Chaos **33**, 033111 (2023).
[33]K. Zhao, Y. Ding, Y. Han, Y. Fan, A. F. Alexander-Bloch *et al.*, Independent and reproducible hippocampal radiomic biomarkers for multisite Alzheimer's disease: Diagnosis, longitudinal progress and biological basis, Sci Bull **65**, 1103 (2020).
[34]J. Li, D. Jin, A. Li, B. Liu, C. Song, P. Wang *et al.*, ASAF: Altered spontaneous activity fingerprinting in Alzheimer's disease based on multisite fMRI, Sci Bull **64**, 998 (2019).
[35]K. Xu, Y. Liu, Y. Zhan, J. Ren, T. Jiang, BRANT: A Versatile and Extendable Resting-State fMRI Toolkit, Front. Neuroinform. **12**, 52 (2018).
[36]J. Liu, X. Zhang, C. Yu, Y. Duan, J. Zhuo, Y. Cui *et al.*, Impaired Parahippocampus connectivity in mild cognitive impairment and Alzheimer's Disease, J. Alzheimer's Dis. **49**, 1051 (2016).
[37]Y. Liu, C. Yu, X. Zhang, J. Liu, Y. Duan, A. F. Alexander-Bloch *et al.*, Impaired long distance functional connectivity and weighted network architecture in Alzheimer's Disease, Cereb. Cortex **24**, 1422 (2014).
[38]H. Zhang, M. Zheng, Y. Zhang, X. Yu, W. Li, H. Gao, Application of ESN prediction model based on compressed sensing in stock market, Commun Nonlinear Sci Numer Simulat **101**, 105857 (2021).
[39]Z. Wang, H. Zhao, M. Zheng, S. Niu, and X. Gao, A novel time series prediction method based on pooling compressed sensing echo state network and its application in stock market, Neural Networks **164**, 216–227 (2023).
[40]H. Kantz, G. Radons, and H. Yang, J. Phys. A: Math. Theor. **46**, 254009 (2013).
[41]T. D. Sauer, J. A. Tempkin, and J. A. Yorke, Phys. Rev. Lett. **81**, 4341 (1998).
[42]H. Abarbanel, Analysis of Observed Chaotic Data (Springer Science & Business Media, 2012).
[43]A. Serrano-Pozo, M. P. Frosch, E. Masliah, B. T. Hyman, Neuropathological Alterations in Alzheimer Disease, Cold Spring Harb Perspect Med **1**, a006189 (2011).
[44]J. Fell and N. Axmacher, The role of phase synchronization in memory processes, Nat. Rev. Neurosci. **12**, 105 (2011).
[45]B. Wang, Y. Niu, L. Miao, R. Cao, P. Yan, H. Guo, D. Li, Y. Guo, T. Yan, J. Wu, J. Xiang, and H. Zhang, Decreased Complexity in Alzheimer's Disease: Resting-State fMRI Evidence of Brain Entropy Mapping, Front. Aging Neurosci. **9**, 378 (2017).
[46]S. L. Warren and A. A. Moustafa, Functional magnetic resonance imaging, deep learning, and Alzheimer's disease: A systematic review, J. Neuroimaging **33**, 5 (2023).
[47]W. Li, X. Lin, X. Chen, Detecting Alzheimer's disease based on 4D fMRI: An exploration under deep learning framework, Neurocomputing **388**, 280 (2020).
[48]H. Lu, S. Liu, H. Wei, C. Chen, X. Geng, Deep multi-kernel auto-encoder network for clustering brain functional connectivity data, Neural Networks **135**, 148 (2021).